# Supporting Information for Muted Equatorial Pacific Carbon Response to the 2023 El Niño

Weixian Zeng[1], Enhui Liao*[1], Xueying Zhang[1], Baoxiao Qu[2,3], Xueming Zhu[4], Guansuo Wang[5,6], Shiyu Liang[7], Alizée Roobaert[8], Jens Daniel Müller[9,10,11], and Cong Guan[12]

[1]State Key Laboratory of Submarine Geoscience; Key Laboratory of Polar Ecosystem and Climate Change; Ministry of Education; Shanghai Key Laboratory of Polar Life and Environment Sciences; and School of Oceanography, Shanghai Jiao Tong University, Shanghai, China
[2]Institute of Oceanology, Chinese Academy of Sciences, Qingdao, China
[3]Center for Ocean Mega-Science, Chinese Academy of Sciences, Qingdao, China
[4]Southern Marine Science and Engineering Guangdong Laboratory (Zhuhai), Zhuhai, China
[5]Observation and Research Station of Huaniaoshan East China Sea Ocean–Atmosphere Integrated Ecosystem, Ministry of Natural Resources, Shanghai, China
[6]East China Sea Forecasting and Hazard Mitigation Center, Ministry of Natural Resources, Shanghai, China
[7]John Hopcroft Center for Computer Science, Shanghai Jiao Tong University, Shanghai, China
[8]Flanders Marine Institute (VLIZ), Ostend, Belgium
[9]Carbon to Sea Initiative, Washington D.C., USA
[10]Climate and Environmental Physics, Physics Institute, University of Bern, Bern, Switzerland
[11]Oeschger Centre for Climate Change Research, University of Bern, Switzerland
[12]College of Oceanography, Hohai University, Nanjing, China

# Contents

**Section S1. Data and model evaluation** **3**

**Section S2 MOM6-COBALT2 model setup** **5**

**Section S3 Air-sea $CO_2$ flux decomposition** **6**

*Correspondence to: ehliao@sjtu.edu.cn

27 **Section S4 Ocean $pCO_2$ decomposition** **8**

28 **Section S5 Figures. S1-S21** **11**

# Section S1. Data and model evaluation

Climatological fields for both the model and observations are calculated over the period from January 1982 to December 2024, except for observational products with shorter temporal coverage. Interannual anomalies are derived through a three-step procedure. First, the long-term trend is removed using a quadratic polynomial fit of the form $ax^2 + bx + c$, fitted over 1982–2024. Second, the climatological monthly mean is subtracted to remove the seasonal cycle. Finally, a 3-month running mean is applied to suppress high-frequency variability. Throughout this study, positive $CO_2$ flux values denote $CO_2$ outgassing from the ocean to the atmosphere.

MOM6-COBALT2 simulations of air-sea $CO_2$ fluxes and sea surface $pCO_2$ are evaluated through comparison with observation-based data products, including SOCAT monthly gridded dataset (Bakker et al., 2016) and multiple independent data products (see Table S1). The simulated sea surface $pCO_2$ exhibits strong coherence with SOCAT-based data reconstructions in both spatial patterns and temporal variability (Fig. S1). In particular, the model realistically reproduces the spatial distribution of oceanic $pCO_2$ in the tropical Pacific, with higher values in the equatorial and central–eastern Pacific and lower values in the western Pacific (Fig. S1a-b). On temporal scales, the model also captures both the long-term trend and the dominant interannual variability, characterized by decreases in oceanic $pCO_2$ during El Niño events and increases during La Niña events (Fig. S1c). This agreement indicates that the model successfully captures the large-scale features of tropical Pacific carbon variability associated with ENSO-driven air–sea $CO_2$ exchange.

To further assess the physical fidelity of the MOM6 model, we compare simulated and observed climatological annual-mean fields of key physical variables, including sea surface temperature (SST), sea surface salinity (SSS), and mixed layer depth (MLD) (Fig. S2). SST observations are obtained from the Optimum Interpolation Sea Surface Temperature (OISST; Huang et al. (2021a)) product, SSS from the Optimum Interpolation analysis of Aquarius sea surface salinity (OISSS; Melnichenko et al. (2016)), and MLD estimates from Argo float profiles (Holte et al., 2017). Overall, the model successfully captures the major large-scale features of the mean state, including the warm SST in the western basin and the relatively cooler conditions in the eastern basin, as well as the low-SSS band associated with the ITCZ, supporting a physically consistent background state suitable for diagnosing interannual anomalies.

Model performance at individual locations is further evaluated using in situ observations from the Tropical Atmosphere Ocean (TAO) array (McPhaden et al., 1998; Sutton et al., 2014), obtained from the NOAA Pacific Marine Environmental Laboratory. We

analyze time series of observed data from five equatorial TAO mooring sites (Fig. S4). The model simulation successfully reproduced the observed variations in SSS and SST in the equatorial Pacific, with a significant rise in SST and decrease in SSS corresponding to the 2023 El Niño. $pCO_2$ simulations are moderately lower than observations, but demonstrate good consistency in temporal variation.

In Fig. S3, we evaluate the climatological annual-mean distributions of key biogeochemical tracers against GLODAP observations, including dissolved inorganic carbon (DIC), total alkalinity (Alk), phosphate ($PO_4$), and nitrate ($NO_3$). The model reproduces realistic basin-scale magnitudes and spatial patterns of these tracers at climatological states, including the dilution associated with the ITCZ band. The close match with observations confirms the model's ability to accurately represent key $CO_2$-related biogeochemical variables.

Finally, we evaluate the model's ability to represent the spatial–temporal evolution of ENSO-related anomalies during the 2023 extreme El Niño by comparing simulated anomalies of SST, SSS, chlorophyll, and sea surface height (SSH) with observations (Figs. S5–S6). The model successfully reproduces the observed progression of large-scale anomaly patterns, including the rapid warming of the central and eastern equatorial Pacific, the associated freshening signals, and the basin-wide sea level response. In particular, both the magnitude and timing of SST and SSH anomalies are well captured, demonstrating that the model realistically represents the key physical processes governing the development and decay of the event. Chlorophyll anomalies are also broadly consistent with observations, although their amplitude is partially overestimated in the equatorial region. Overall, these evaluations confirm that MOM6-COBALT2 provides a credible representation of the 2023 El Niño evolution, supporting its use for investigating the mechanisms underlying the muted tropical Pacific $CO_2$ flux response. A companion simulation with nearly identical physics has previously been validated and applied to study $CO_2$ flux variability in the tropical Pacific (Liao et al., 2020).

To further evaluate the ability of data-driven products and numerical models to reproduce the carbon response to the 2023 El Niño, we analysed the relationship between SST and air–sea $CO_2$ flux ($FCO_2$) in the equatorial Pacific over the period 1982–2024 (Friedlingstein et al. (2025); Fig. S11). A detailed description of the datasets is provided in Table S1. For each dataset, a linear regression was performed with respect to the Niño3.4 index. To quantify how well each dataset captures deviations from the conventional SST–$FCO_2$ coupling, the departure of the 2023 value from the fitted regression was characterized using both the residual ($r$) and the standardized residual ($z$), where $z$ represents the number of standard deviations by which the 2023 observation departs from the expected linear relationship. Overall, model simulations outperform

| | Dataset | Data type | Reference |
|---|---|---|---|
| 1 | SJTU-AViT | Obs-based product | Zhang et al. (2025) |
| 2 | VLIZ-SOMFFN | Obs-based product | Landschützer et al. (2020) |
| 3 | JENA-MLS | Obs-based product | Rödenbeck et al. (2022) |
| 4 | JMA-MLR | Obs-based product | Iida et al. (2015) |
| 5 | CSIR-ML6 | Obs-based product | Gregor et al. (2019) |
| 6 | UExP-FNN-U | Obs-based product | Ford et al. (2024) |
| 7 | LDEO-HPD | Obs-based product | Bennington et al. (2022) |
| 8 | NIES-ML3 | Obs-based product | Zeng (2022) |
| 9 | CMEMS-LSCE-FFNN | Obs-based product | Chau et al. (2024) |
| 10 | OceanSODA-ETHZv2 | Obs-based product | Gregor and Gruber (2021) |
| 11 | FESOM | Model simulation | Gürses et al. (2023) |
| 12 | IPSL | Model simulation | Aumont et al. (2015) |
| 13 | PRINCETON | Model simulation | Liao et al. (2020) |
| 14 | CESM | Model simulation | Doney et al. (2009) |
| 15 | CNRM | Model simulation | Séférian et al. (2019); Berthet et al. (2019) |
| 16 | ACCESS | Model simulation | Law et al. (2017) |
| 17 | PLANKTOM | Model simulation | Wright et al. (2021) |
| 18 | MRI | Model simulation | Tsujino et al. (2020) |
| 19 | MPI | Model simulation | Lacroix et al. (2021) |
| 20 | NORESM | Model simulation | Schwinger et al. (2016) |

**Table S1.** Description of observation-based data products and model simulations used for MOM6 validation.

data-driven products in reproducing the anomalous carbon signal associated with the 2023 El Niño event. In half of the machine learning based data products, the standard residual in 2023 exceeded 1, while 6 out of 10 model simulations reported a similar phenomenon. To assess the robustness of the results, tropical Pacific $FCO_2$ time series are derived using both linearly and quadratically detrended data (Fig. S21). The close agreement between the two approaches confirms the stability of the inferred variability.

# Section S2 MOM6-COBALT2 model setup

In this work, we employ the coupled ocean–sea ice–biogeochemistry modeling framework developed at the Geophysical Fluid Dynamics Laboratory (GFDL). The physical circulation is represented by the Modular Ocean Model version 6 (MOM6) in combination with the Sea Ice Simulator version 2 (SIS2). We adopt the OM4p5 configuration,

which has a nominal 0.5° horizontal grid spacing and applies eddy parameterizations (see Adcroft et al. (2019) for further details). Biogeochemistry is simulated with the Carbon, Ocean Biogeochemistry, and Lower Trophics module version 2 (COBALT2), which explicitly resolves 33 tracers. These tracers encompass the major nutrients (nitrate, phosphate, silicate, and iron), dissolved oxygen, carbonate system variables, three functional groups of phytoplankton, three zooplankton size classes, three pools of dissolved organic matter, and a single detrital pool (Stock et al., 2020). A comprehensive description of the trophic interactions and global carbon cycling represented by COBALT2 can be found in Stock et al. (2020).

The ocean model is driven by the Japanese 55-year atmospheric reanalysis forcing dataset (JRA55-do v1.5; Tsuji et al. (2018)) and by atmospheric deposition fluxes of iron, lithogenic material, phosphate, and reactive nitrogen ($NO_3$, $NH_4$) from the GFDL-ESM4 simulations. The coupled system is spun up from rest for 81 years using a repeated cycle of 1959 JRA55-do v1.5 forcing. The imposed atmospheric $CO_2$ is taken from the Global Carbon Budget dataset (Friedlingstein et al., 2025), which merges Mauna Loa and South Pole observations into a globally averaged monthly time series. Initial fields of temperature, salinity, nutrients (nitrate, phosphate, silicate), and oxygen are derived from the World Ocean Atlas 2013 (Locarnini et al., 2013; Zweng et al., 2013; Garcia et al., 2013a,b). DIC and Alk initial conditions are based on GLODAPv2 (Lauvset et al., 2022), with DIC adjusted for anthropogenic carbon accumulation to represent conditions in 1959 following the data-based estimates of Khatiwala et al. (2013). Remaining COBALT tracers (e.g., ammonium, calcium carbonate) are initialized from a preindustrial GFDL-ESM2M–COBALT simulation (Stock et al., 2014).

# Section S3 Air-sea $CO_2$ flux decomposition

The air-sea $CO_2$ flux is computed from the air-sea $pCO_2$ gradient and a gas transfer coefficient determined by wind speed and temperature:

$$\mathrm{FCO_2} = k_w \alpha (p\mathrm{CO_{2w}} - p\mathrm{CO_{2a}}) = K \Delta p\mathrm{CO_2} \tag{S1}$$

where $p\mathrm{CO_{2w}}$ and $p\mathrm{CO_{2a}}$ denote the partial pressures of CO2 in sea surface and the atmosphere, respectively. The term $\alpha$ is the solubility of $CO_2$, computed as a function of temperature and salinity following the formulation of Weiss and Price (1980), and $k_w$ is the gas transfer velocity, calculated using a quadratic wind-speed parameterization (Wanninkhof et al., 2013). The implementation of both coefficients follows the approach described by Najjar and Orr (1998). Positive values of $FCO_2$ indicate net outgassing

of $CO_2$ from the ocean to the atmosphere. For simplicity, the product $k_w\alpha$ is combined into a single bulk gas transfer coefficient, $K$. The term $\Delta pCO_2$ represents the air–sea difference in CO2 partial pressure, defined as $pCO_{2w} - pCO_{2a}$.

To calculate the variation in air-sea $CO_2$ flux, the Reynolds average is applied to $K$ and $\Delta pCO_2$. By removing the seasonality and quadratic trend, it yields the following decomposition of $K$ and $\Delta pCO_2$:

$$K = \overline{K} + K' \tag{S2}$$

$$\Delta pCO_2 = \overline{\Delta pCO_2} + \Delta pCO_2' \tag{S3}$$

where $\overline{K}$ and $\overline{\Delta pCO_2}$ represents long-term mean $K$ and $\Delta pCO_2$, and $K'$ and $\Delta pCO_2$ represents the interannual flucuations. Based on this simplification, air-sea $CO_2$ flux can be represented as:

$$\begin{aligned} FCO_2 &= K\Delta pCO_2 = (\overline{K} + K')(\overline{\Delta pCO_2} + \Delta pCO_2') \\ &= \overline{K}\,\overline{\Delta pCO_2} + K'\,\overline{\Delta pCO_2} + \overline{K}\,\Delta pCO_2' + K'\,\Delta pCO_2' \end{aligned} \tag{S4}$$

which derives the long-term mean air-sea $CO_2$ flux:

$$\overline{FCO_2} = \langle FCO_2 \rangle = \langle \overline{K}\ \ \overline{\Delta pCO_2} \rangle + \langle K'\,\overline{\Delta pCO_2} \rangle + \langle \overline{K}\,\Delta pCO_2' \rangle + \langle K'\,\Delta pCO_2' \rangle \tag{S5}$$

where angle brackets are used to denote the average. Assuming the interannual anomaly is randomly distributed, and we have:

$$\begin{aligned} \langle K'\,\overline{\Delta pCO_2} \rangle &= 0 \cdot \overline{\Delta pCO_2} = 0 \\ \langle \overline{K}\,\Delta pCO_2' \rangle &= \overline{K} \cdot 0 = 0 \\ \langle \overline{K}\ \ \overline{\Delta pCO_2} \rangle &= \overline{K}\ \ \overline{\Delta pCO_2} \\ \langle K'\,\Delta pCO_2' \rangle &= \langle K'\,\Delta pCO_2' \rangle \end{aligned} \tag{S6}$$

Thus, the interannual variation of air-sea $CO_2$ flux can be calculated as:

$$\begin{aligned} FCO_2' &= FCO_2 - \overline{FCO_2} \\ &= \overline{K}\,\overline{\Delta pCO_2} + K'\,\overline{\Delta pCO_2} + \overline{K}\,\Delta pCO_2' + K'\,\Delta pCO_2' \\ &\quad - \langle \overline{K}\ \ \overline{\Delta pCO_2} \rangle - \langle K'\,\overline{\Delta pCO_2} \rangle - \langle \overline{K}\,\Delta pCO_2' \rangle - \langle K'\,\Delta pCO_2' \rangle \\ &= \underbrace{K'\overline{\Delta pCO_2}}_{FCO_2-GT} + \underbrace{\overline{K}\Delta pCO_2'}_{FCO_2-BGC} + RES \end{aligned} \tag{S7}$$

where $RES$ represents the small residual of the cross terms ($K'\,\Delta p\mathrm{CO}_2' - \langle K'\,\Delta p\mathrm{CO}_2' \rangle$). The variation in $\mathrm{CO}_2$ flux is thus separated into two components, the wind-driven term and the $p\mathrm{CO}_2$ driven term.

# Section S4 Ocean $p\mathrm{CO}_2$ decomposition

The variability of oceanic partial pressure of $\mathrm{CO}_2$ ($p\mathrm{CO}_2$) can be decomposed into contributions from changes in DIC, alkalinity (Alk), temperature (T), and salinity (S), following the linear approximation proposed by Takahashi et al. (1993) and Le Quéré et al. (2000). The change in oceanic $p\mathrm{CO}_2$, denoted as $\Delta pCO_{2,w}$, can be expressed as:

$$\Delta p\mathrm{CO}_{2w} \approx \underbrace{\frac{\partial p\mathrm{CO}_{2w}}{\partial T}\Delta T}_{p\mathrm{CO}_2-T} + \underbrace{\frac{\partial p\mathrm{CO}_{2w}}{\partial \mathrm{DIC}}\Delta\mathrm{DIC} + \frac{\partial p\mathrm{CO}_{2w}}{\partial \mathrm{Alk}}\Delta\mathrm{Alk} + \frac{\partial p\mathrm{CO}_{2w}}{\partial \mathrm{S}}\Delta\mathrm{S}}_{p\mathrm{CO}_2-\mathrm{NONT}} \tag{S8}$$

Where $\Delta\mathrm{pCO}_{2w}$ denotes the ocean $p\mathrm{CO}_2$. Among the four main factors, the $\Delta T$ term is identified as the thermal component ($p\mathrm{CO}_2 - T$), and the $p\mathrm{CO}_2$ change derived from the other tracers ($\Delta$DIC, $\Delta$Alk, and $\Delta$S) forms the non-thermal component ($p\mathrm{CO}_2 - T$).

Taking the total time derivative of Eq. (S8), a tracer-based decomposition of ocean $p\mathrm{CO}_2$ budget is represented as:

$$\partial_t p\mathrm{CO}_{2w} \approx \frac{\partial p\mathrm{CO}_{2w}}{\partial \mathrm{T}}\,\partial_t\mathrm{T} + \frac{\partial p\mathrm{CO}_{2w}}{\partial \mathrm{DIC}}\,\partial_t\mathrm{DIC} + \frac{\partial p\mathrm{CO}_{2w}}{\partial \mathrm{Alk}}\,\partial_t\mathrm{Alk} + \frac{\partial p\mathrm{CO}_{2w}}{\partial \mathrm{S}}\,\partial_t\mathrm{S} \tag{S9}$$

To further investigate the sources of variability in each tracer (DIC, Alk, T, and S), their temporal evolution is attributed to several key oceanic processes, including horizontal and vertical transport, biological activity, air–sea gas exchange, and surface forcing (Liao et al., 2024; Sun et al., 2025). The general tracer budgets for the scalar quantities can be written as:

$$\begin{aligned}
\partial_t\mathrm{T} &\approx \mathrm{T}_H + \mathrm{T}_V + \mathrm{T}_Q \\
\partial_t\mathrm{DIC} &\approx \mathrm{DIC}_H + \mathrm{DIC}_V + \mathrm{DIC}_{FCO_2} + \mathrm{DIC}_{Bio} + \mathrm{DIC}_{FW} \\
\partial_t\mathrm{Alk} &\approx \mathrm{Alk}_H + \mathrm{Alk}_V + \mathrm{Alk}_{Bio} + \mathrm{Alk}_{FW} \\
\partial_t\mathrm{S} &\approx \mathrm{S}_H + \mathrm{S}_V + \mathrm{S}_{FW}
\end{aligned} \tag{S10}$$

where the $H$ terms represent contributions of horizontal transport processes, the $V$ terms indicate vertical advection, $FCO_2$ in the DIC equation accounts for variations due to air-sea gas exchange, the $Bio$ terms encapsulate the effects of biological processes, and the $Q$ term in the temperature equations reflects the impact of surface heat flux. The $FW$ terms represent the effects of freshwater inputs from rainfall, rivers, and sea ice, which modulate DIC/Alk/S through dilution and concentration processes.

Substituting the tracer tendency equations in Eq. S10 into Eq. S9 yields

$$\begin{aligned}\partial_t pCO_{2w} \approx & \frac{\partial pCO_{2w}}{\partial T}(T_H + T_V + T_Q) \\ & + \frac{\partial pCO_{2w}}{\partial DIC}(DIC_H + DIC_V + DIC_{FCO_2} + DIC_{Bio} + DIC_{FW}) \\ & + \frac{\partial pCO_{2w}}{\partial Alk}(Alk_H + Alk_V + Alk_{Bio} + Alk_{FW}) \\ & + \frac{\partial pCO_{2w}}{\partial S}(S_H + S_V + S_{FW}).\end{aligned} \tag{S11}$$

Time tendency of $pCO_{2w}$ is referred to as the $pCO_2$ response. To isolate and quantify the non-thermal mechanisms driving changes in ocean $pCO_{2w}$ ($\partial_t pCO_{2w-nonT}$), Eq. S11 can be regrouped into process-level budgets:

$$\begin{aligned}\partial_t pCO_{2w-nonT} \approx & \underbrace{\left(\frac{\partial pCO_{2w}}{\partial DIC} DIC_H + \frac{\partial pCO_{2w}}{\partial Alk} Alk_H + \frac{\partial pCO_{2w}}{\partial S} S_H\right)}_{H_{circ}} \\ & + \underbrace{\left(\frac{\partial pCO_{2w}}{\partial DIC} DIC_V + \frac{\partial pCO_{2w}}{\partial Alk} Alk_V + \frac{\partial pCO_{2w}}{\partial S} S_V\right)}_{V_{circ}} \\ & + \underbrace{\left(\frac{\partial pCO_{2w}}{\partial DIC} DIC_{FW} + \frac{\partial pCO_{2w}}{\partial Alk} Alk_{FW} + \frac{\partial pCO_{2w}}{\partial S} S_{FW}\right)}_{FW} \\ & + \underbrace{\left(\frac{\partial pCO_{2w}}{\partial DIC} DIC_{Bio} + \frac{\partial pCO_{2w}}{\partial Alk} Alk_{Bio}\right)}_{Bio} + \underbrace{\left(\frac{\partial pCO_{2w}}{\partial DIC} DIC_{FCO_2}\right)}_{Flux\ response}\end{aligned} \tag{S12}$$

where the non-thermal changes in ocean surface $pCO_{2w}$ (left-hand side) are decomposed into contributions from individual processes (right-hand side): horizontal transport ($H_{circ}$), vertical advection ($V_{circ}$), freshwater fluxes (FW), biological uptake ($Bio$), thermal effects (Thermal), and its flux response (Flux response).

Similar to Eq. S12, the thermal-induced temporal change in $pCO_{2w}$ ($\partial_t pCO_{2w-T}$) can be represented as:

$$\begin{aligned}\partial_t pCO_{2w-T} \approx & \frac{\partial pCO_{2w}}{\partial T}(T_H + T_V + T_Q) \\ = & \underbrace{\left(\frac{\partial pCO_{2w}}{\partial T} T_H\right)}_{T_{Hcirc}} + \underbrace{\left(\frac{\partial pCO_{2w}}{\partial T} T_V\right)}_{T_{Vcirc}} + \underbrace{\left(\frac{\partial pCO_{2w}}{\partial T} T_Q\right)}_{T_{flux}}\end{aligned} \tag{S13}$$

where the $pCO_{2w-T}$ tendency is attributed to three processes: horizontal and vertical transport of temperature ($T_{Hcirc}$, $T_{Vcirc}$), and surface heat flux ($T_{flux}$).

This decomposition framework (Eqs. S12 and S13) allows a quantitative assessment of the contribution of each physical and biogeochemical process to surface ocean $pCO_2$ variability. In the following sections, it is applied to evaluate the dominant drivers of the carbon anomaly observed during the 2023 El Niño.

The coefficients used for the $pCO_{2w}$ dependence on DIC, alkalinity, salinity, and temperature are approximated by the following equations (Lovenduski et al., 2007; Sarmiento and Gruber, 2013):

$$\begin{aligned}\frac{\partial pCO_{2w}}{\partial DIC} &\approx \frac{\overline{pCO_{2w}}}{\overline{DIC}} \frac{3 \times \overline{Alk} \times \overline{DIC} - 2 \times \overline{DIC}^2}{(2 \times \overline{DIC} - \overline{Alk})(\overline{Alk} - \overline{DIC})} \\ \frac{\partial pCO_{2w}}{\partial Alk} &\approx -\frac{\overline{pCO_{2w}}}{\overline{Alk}} \frac{\overline{Alk}^2}{(2 \times \overline{DIC} - \overline{Alk})(\overline{Alk} - \overline{DIC})} \\ \frac{\partial pCO_{2w}}{\partial T} &\approx \overline{pCO_{2w}} \times 0.0423 \\ \frac{\partial pCO_{2w}}{\partial S} &\approx \frac{\overline{pCO_{2w}}}{\overline{S}}\end{aligned} \tag{S14}$$

Here, overbars denote the annual mean values for the period 1982–2024, and the coefficients are assumed to be time invariant. The coefficients associated with DIC and salinity are positive, indicating that increases in DIC or salinity lead to increases in $pCO_{2w}$. In contrast, the coefficient for alkalinity is negative, implying that higher alkalinity reduces $pCO_{2w}$. Although variations in DIC and alkalinity often exert opposing influences on $pCO_{2w}$, the effect of DIC typically dominates because of its larger sensitivity coefficient.

All terms in Eqs. S12 and S13 are evaluated within the mixed layer. The mixed layer depth is defined as the depth at which seawater density exceeds the surface density by 0.01 kg $m^{-3}$.

# Section S5 Figures. S1-S21

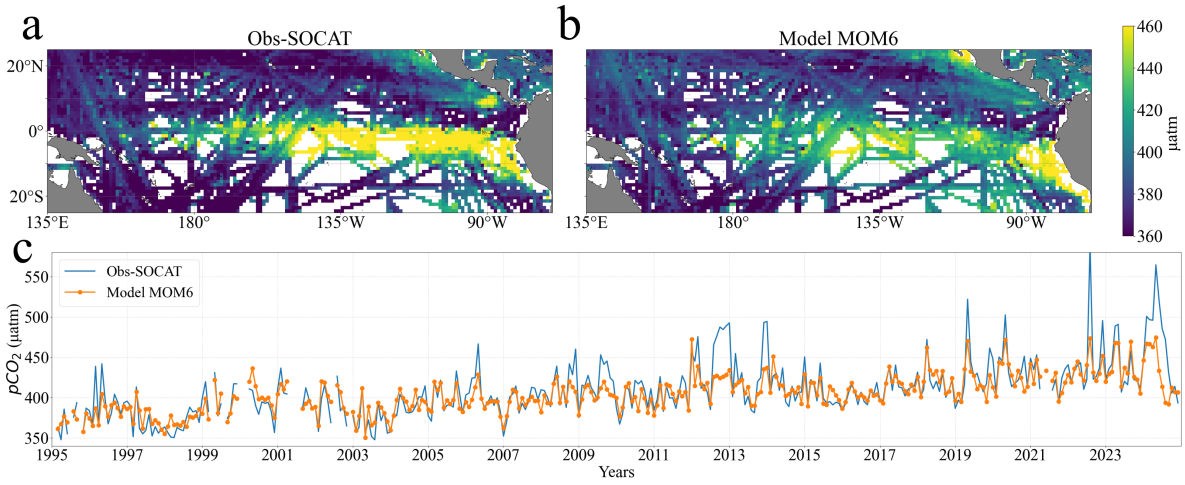



**Figure S1.** Comparison of climatological mean sea surface $pCO_2$ from (a) SOCAT observations (Bakker et al., 2016) and (b) MOM6-COBALT2 simulations, both calculated using only the spatial and temporal sampling of available SOCAT observations during 1995–2024. (c) Time series of basin-mean $pCO_2$, derived from SOCAT observation points within the tropical Pacific (160°E–285°E, 15°S–15°N), with the model sampled at the same locations and times.

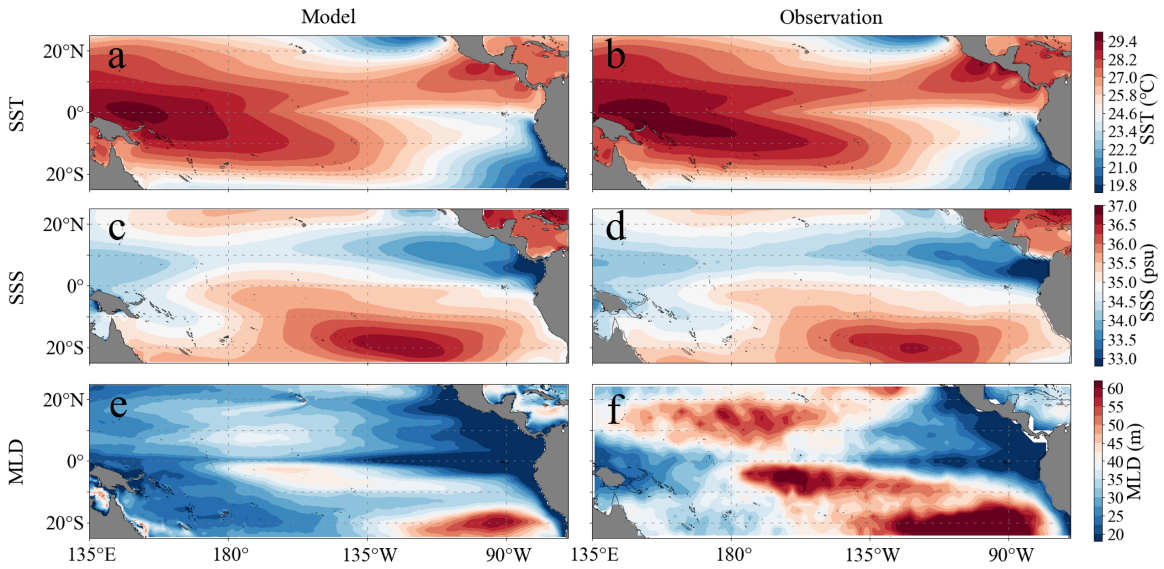



**Figure S2.** Comparison of climatological mean fields in the tropical Pacific between MOM6-COBALT2 simulations (left column) and observations (right column): SST (a, b), SSS (c, d), and MLD (e, f). Observed SST is from OISST v2 (Huang et al., 2021a), SSS from OISSS (Melnichenko et al., 2016), and mixed layer depth from Argo profiles (Holte et al., 2017). The climatological means of each variable are calculated over the full temporal coverage of the corresponding dataset: 1982–2024 for SST, 2011–2024 for SSS, and 2000–2024 for MLD.

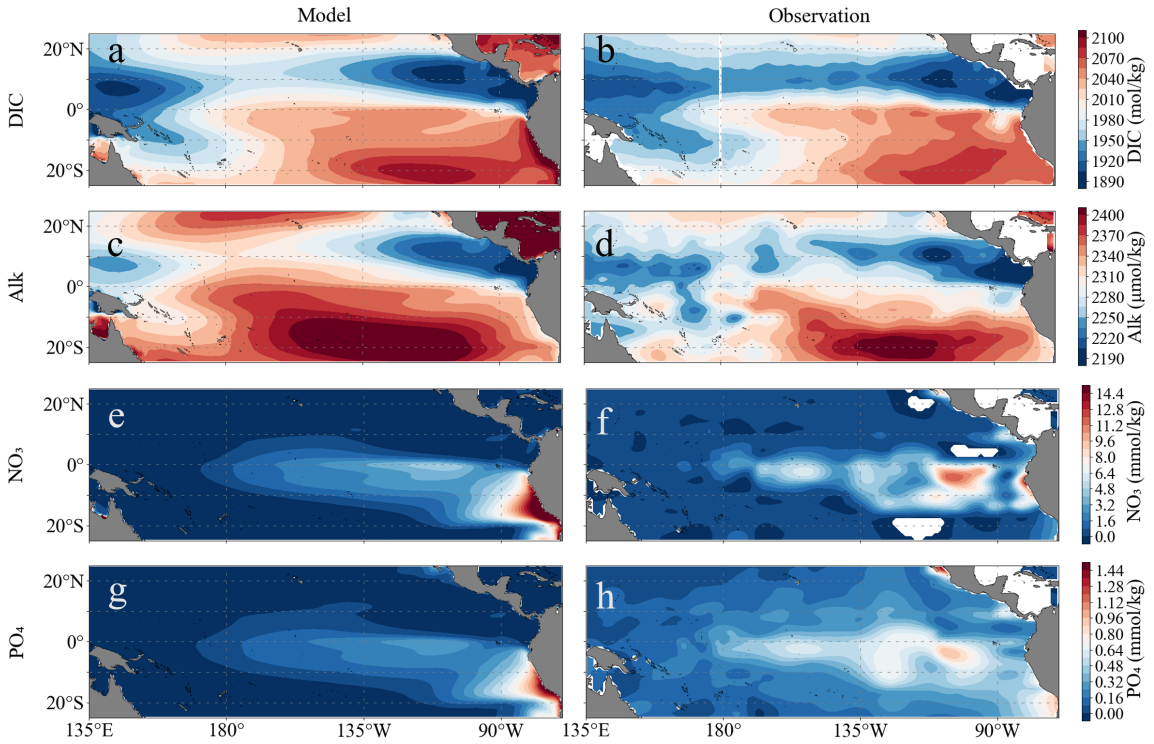



**Figure S3.** Comparison of climatological mean fields in the tropical Pacific between MOM6-COBALT2 simulations (left column) and observations (right column): DIC (a, b), Alk (c, d), $PO_4$ (e, f), and $NO_3$ (g, h). Observational fields of DIC, Alk, $PO_4$, and $NO_3$ are from the WOA 2023 data product. Model climatologies represent the mean over 1982–2024.

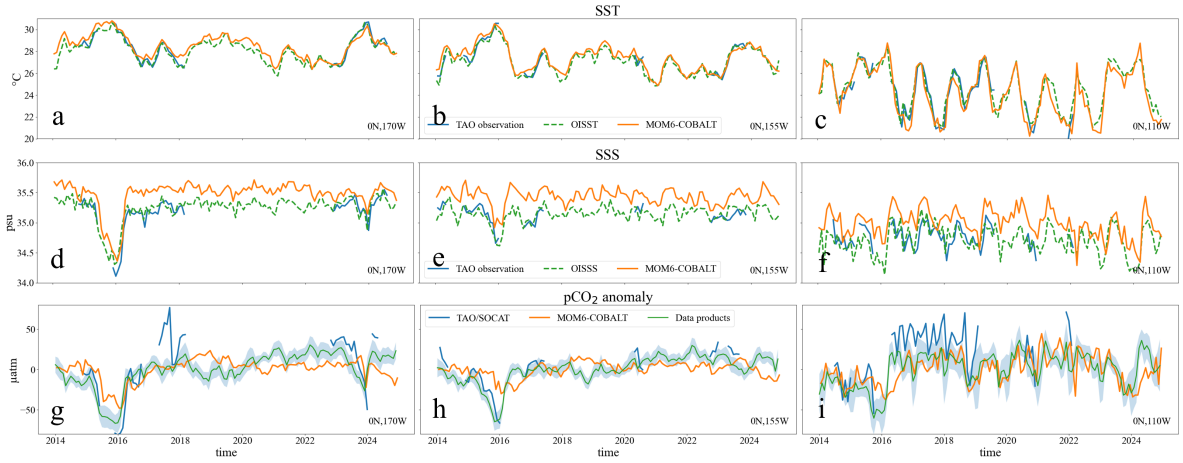



**Figure S4.** Comparison of interannual variability at three TAO mooring stations in the tropical Pacific between MOM6–COBALT2 simulations and observations: SST (a–c), SSS (d–f), and sea-surface $pCO_2$ anomalies (g–i). Each row corresponds to a different mooring location, as indicated in the individual panels. Observations are derived from TAO measurements and observation-based products. Both the observation-based products and MOM6–COBALT2 simulations are interpolated to the TAO locations. Observed SST data product is from OISST v2 (Huang et al., 2021a), SSS data product is from OISSS (Melnichenko et al., 2016), and $pCO_2$ anomalies are from an ensemble of ten observation-based products (see details in Table S1).

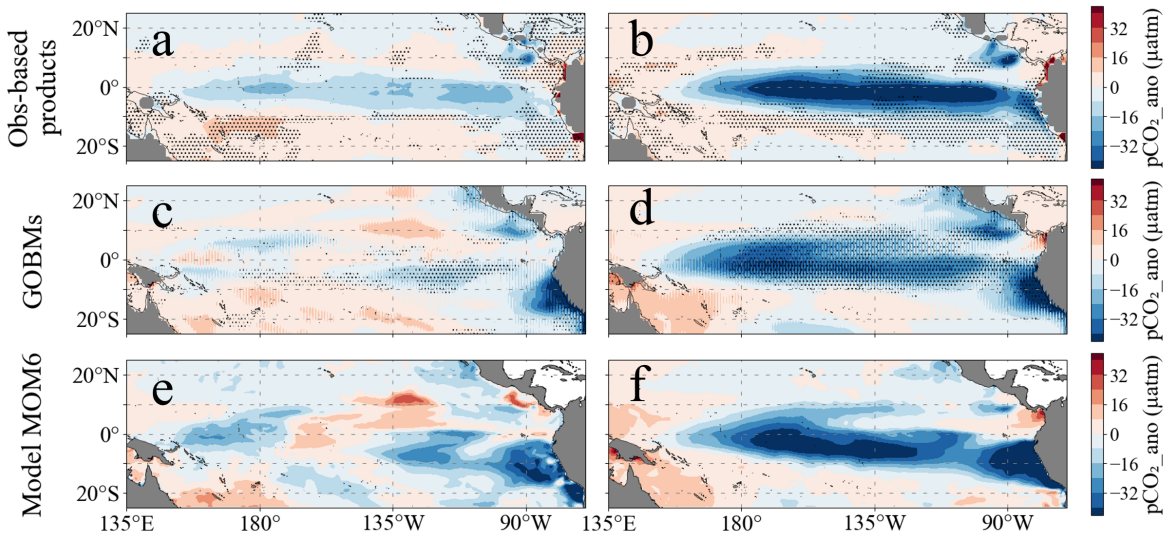



**Figure S5.** Distribution of $pCO_2$ anomalies during the December–February (DJF) of 1997, 2015, and 2023 events from the ensemble mean of (a-b) ten observation-based $fCO_2$ products, (c-d)ten GOBMs, and (e-f)MOM6–COBALT2 simulations. Stippling indicates regions where the inter-product spread (0.2 standard deviation) exceeds the magnitude of the ensemble-mean anomaly. Dataset details are provided in the Methods and Section S1.

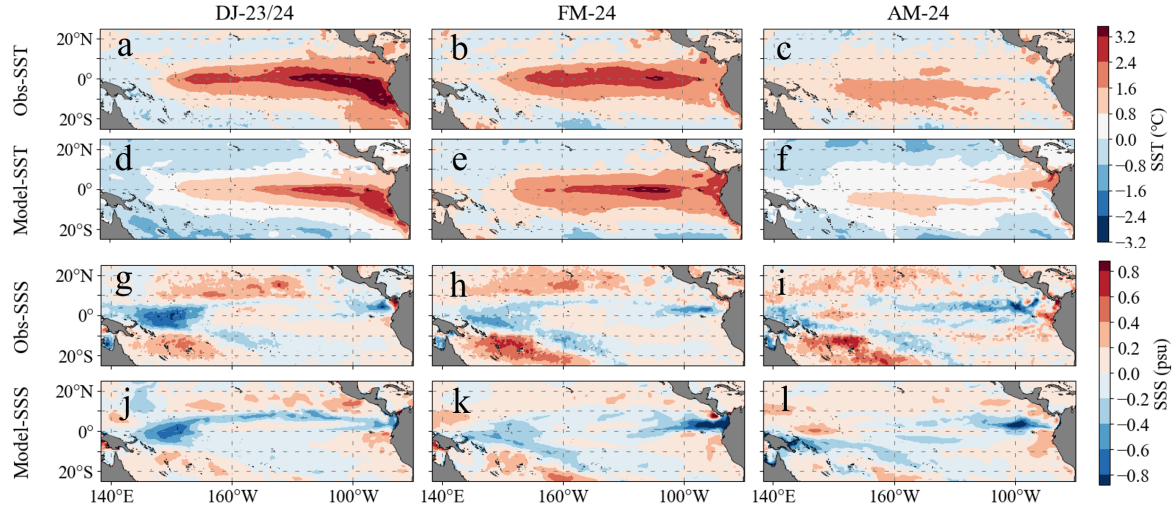



**Figure S6.** Comparison of observed and modeled seasonal evolution of interannual anomalies during the 2023 El Niño for SST (a–f) and SSS (g–l). Observed fields are shown in panels (a–c) and (g–i) from OISST (Huang et al., 2021b) and OISSS (Melnichenko et al., 2016), and corresponding MOM6-COBALT2 simulations in panels (d–f) and (j–l). Columns represent seasonal means for December–January 2023/24 (DJ-23/24), February–March 2024 (FM-24), and April–May 2024 (AM-24), respectively.

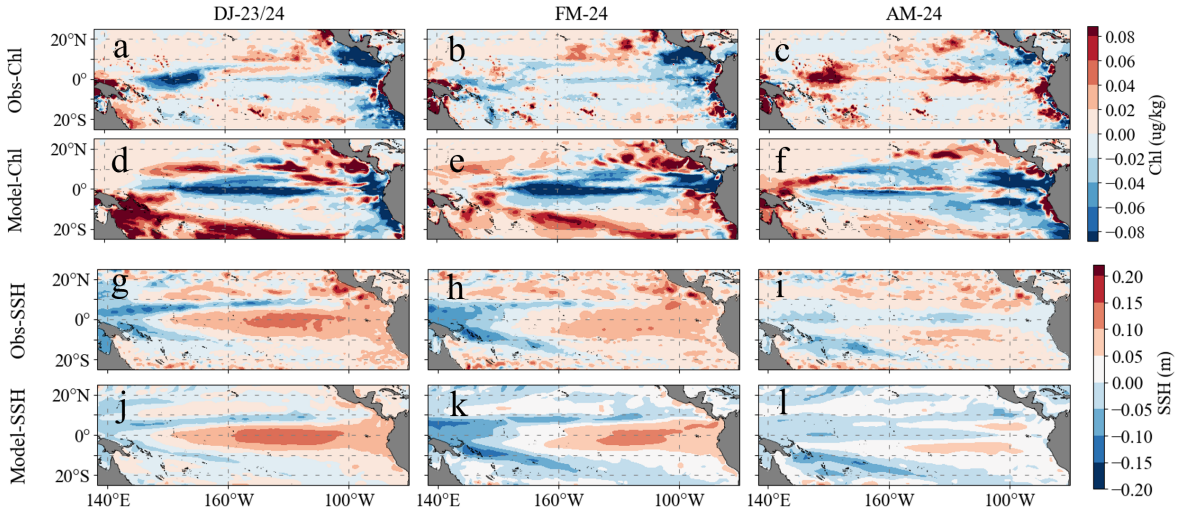



**Figure S7.** Comparison of observed and modeled seasonal evolution of interannual anomalies during the 2023 El Niño for chlorophyll (a–f) and SSH (g–l). Observed fields are shown in panels (a–c) and (g–i) from OC-CCI and satellite altimetry, respectively, and corresponding MOM6-COBALT2 simulations in panels (d–f) and (j–l). Columns represent seasonal means for December–January 2023/24 (DJ-23/24), February–March 2024 (FM-24), and April–May 2024 (AM-24), respectively. The OC-CCI chlorophyll is from Sathyendranath et al. (2019) and the AVISO SSH is from Ducet et al. (2000).

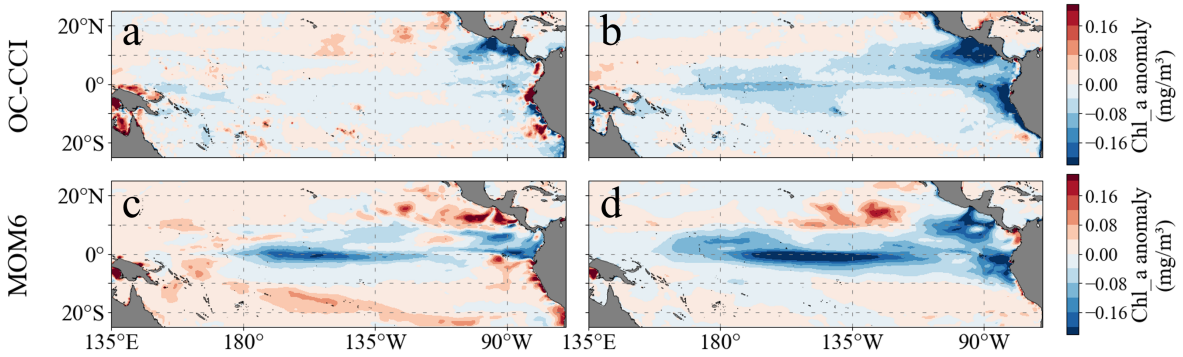



**Figure S8.** Spatial distribution of chlorophyll-*a* (Chl-*a*) anomalies in the tropical Pacific. The left panels show anomalies during the 2023 El Niño, while the right panels present the composite mean anomalies of the 1997 and 2015 events averaged over December–February. Panels (a,b) are derived from OC-CCI observations (Sathyendranath et al., 2019), and panels (c,d) show results from MOM6 simulations.

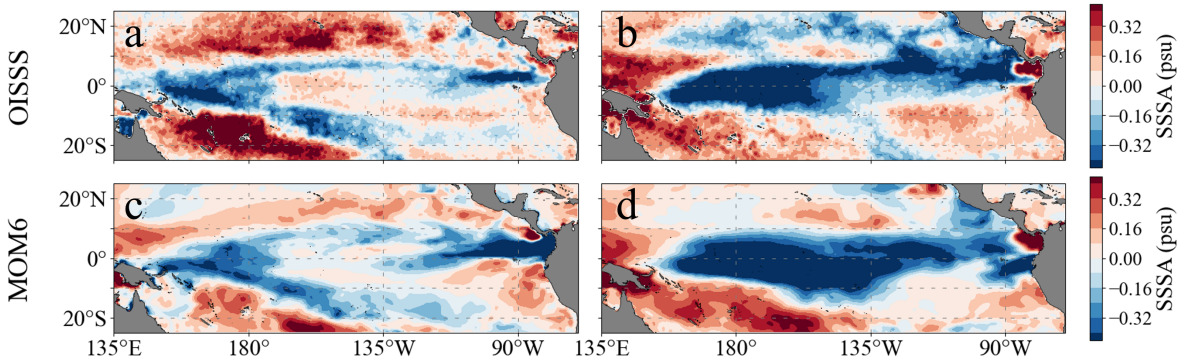



**Figure S9.** Spatial distribution of SSS anomalies in the tropical Pacific. Left panels show anomalies during the 2023 El Niño, while right panels show the composite mean anomalies for the 1997 and 2015 events averaged over December–February. (a,b) are derived from OISSS observations (Melnichenko et al., 2016), while (c,d) are MOM6 simulations.

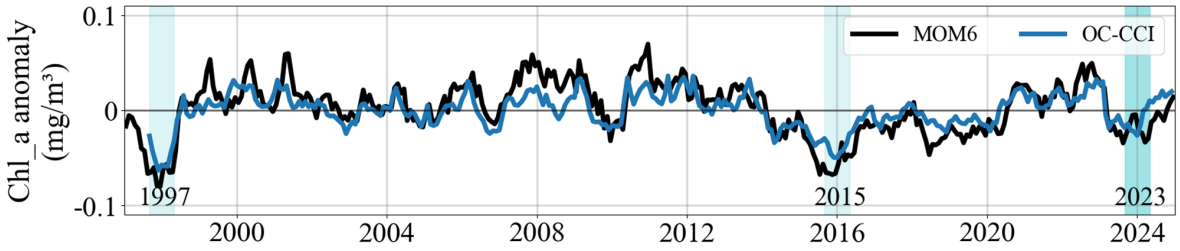



**Figure S10.** Time series of tropical Pacific (160°E-185°E, 15°S-15°N) chlorophyll-*a* anomalies from 1995 to 2024, based on MOM6 simulations and OC-CCI observations.

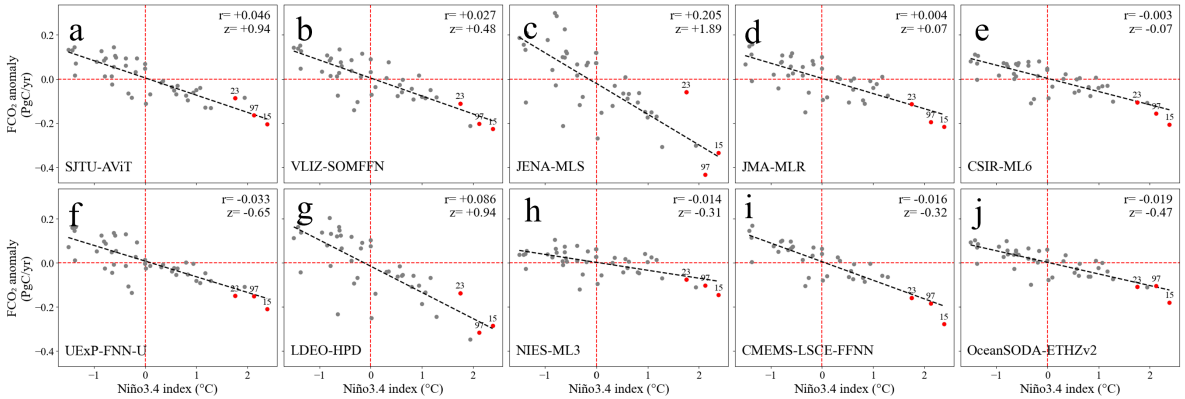



**Figure S11.** Scatter diagrams of the tropical Pacific Sep-Mar $FCO_2$ and the Niño 3.4 index during 1980–2025, based on data-driven observational products. The black dashed line denotes the linear regression between the Niño 3.4 index and the regionally integrated $FCO_2$ anomaly, both calculated for September–March and integrated over 160°E–285°E and 15°S–15°N. Strong El Niño years (1997, 2015, and 2023) are labeled red. $r$ and $z$ scores represent the bias of the 2023 event from the historical SST-$FCO_2$ relationship. All data products are quadratically detrended. See data product details in Table S1.

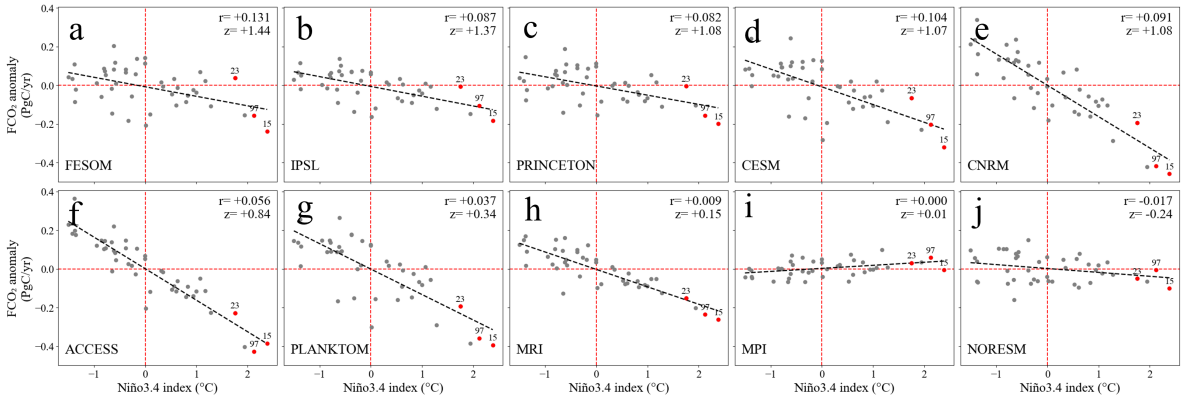



**Figure S12.** Scatter diagrams of the tropical Pacific Sep–Mar $FCO_2$ and the Niño 3.4 index during 1980–2025, based on model simulations. The black dashed line denotes the linear regression between the Niño 3.4 index and the regionally integrated $FCO_2$ anomaly, both calculated for September–March and integrated over 160°E–285°E and 15°S–15°N. Strong El Niño years (1997, 2015, and 2023) are labeled red. $r$ and $z$ scores represent the bias of the 2023 event from the historical SST-$FCO_2$ relationship. All model simulations are quadratically detrended. See model details in Table S1.

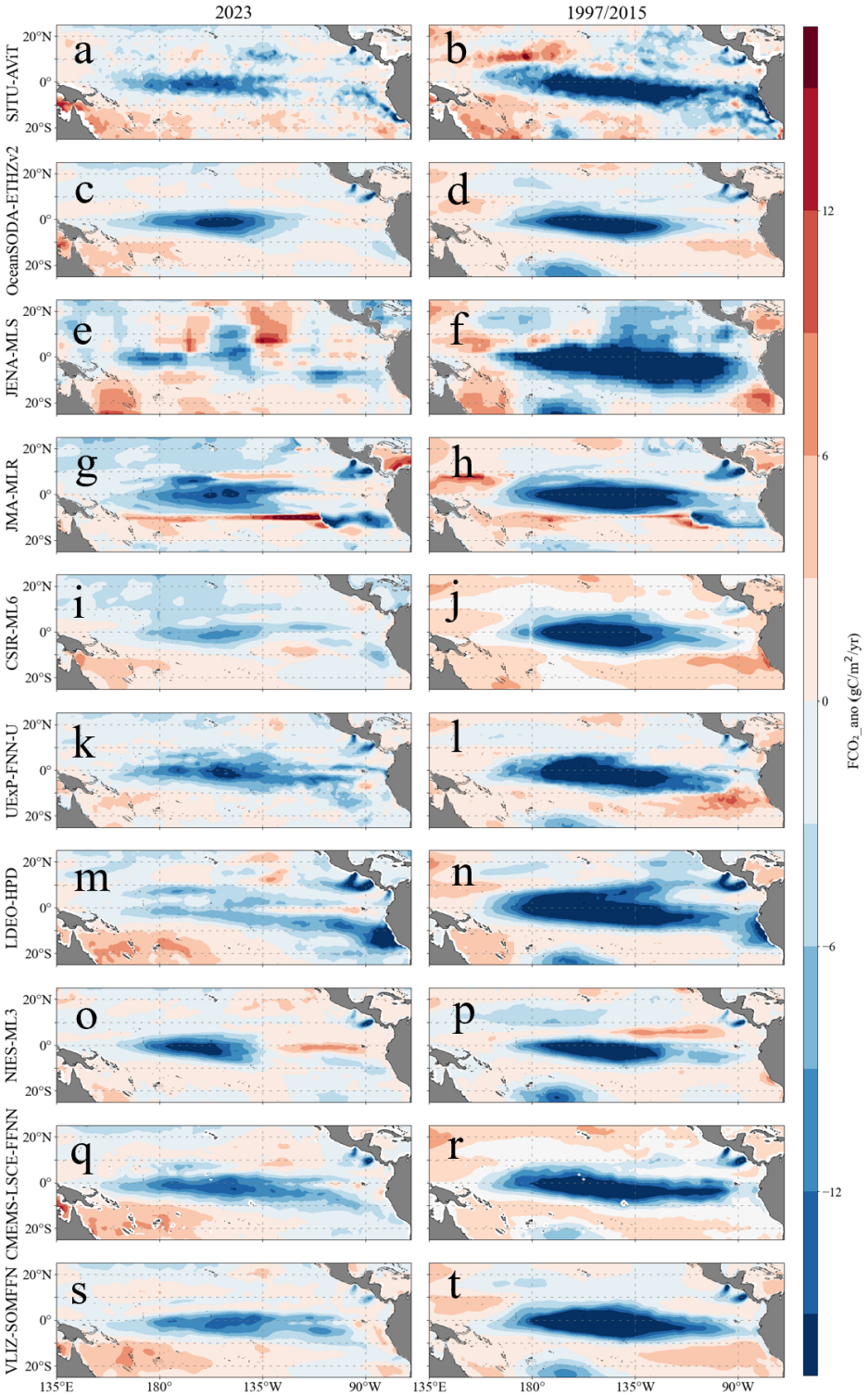



**Figure S13.** Spatial distribution of air–sea $CO_2$ flux ($FCO_2$) anomalies relative to the climatological mean (1980-2024), derived from data-driven products. Left panels show anomalies during the 2023 El Niño event, while right panels display the composite mean anomalies for the 1997 and 2015 El Niño events averaged over December–February.

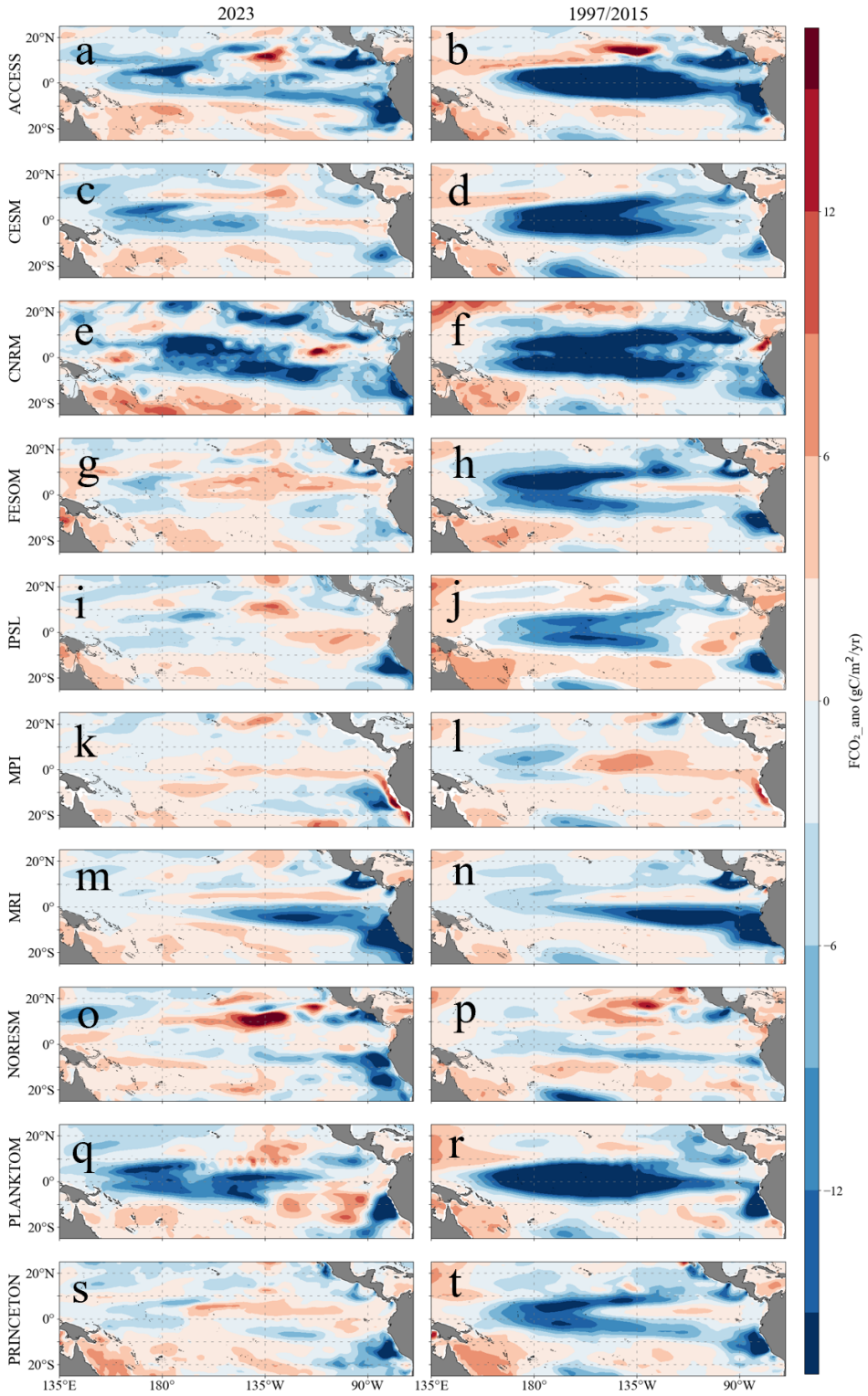



**Figure S14.** Spatial distribution of air–sea $CO_2$ flux ($FCO_2$) anomalies relative to the climatological mean (1980-2024), derived from model simulations. Left panels show anomalies during the 2023 El Niño event, while right panels display the composite mean anomalies for the 1997 and 2015 El Niño events averaged over December–February.

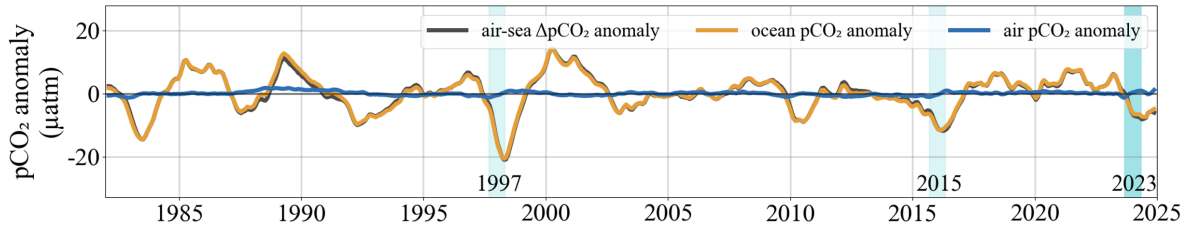



**Figure S15.** Temporal evolution of air–sea $\Delta pCO_2$, oceanic $pCO_2$, and atmospheric $pCO_2$ anomalies averaged over the tropical Pacific (160°E–285°E, 15°S–15°N) for 1982–2025. Vertical shaded regions denote major El Niño events.

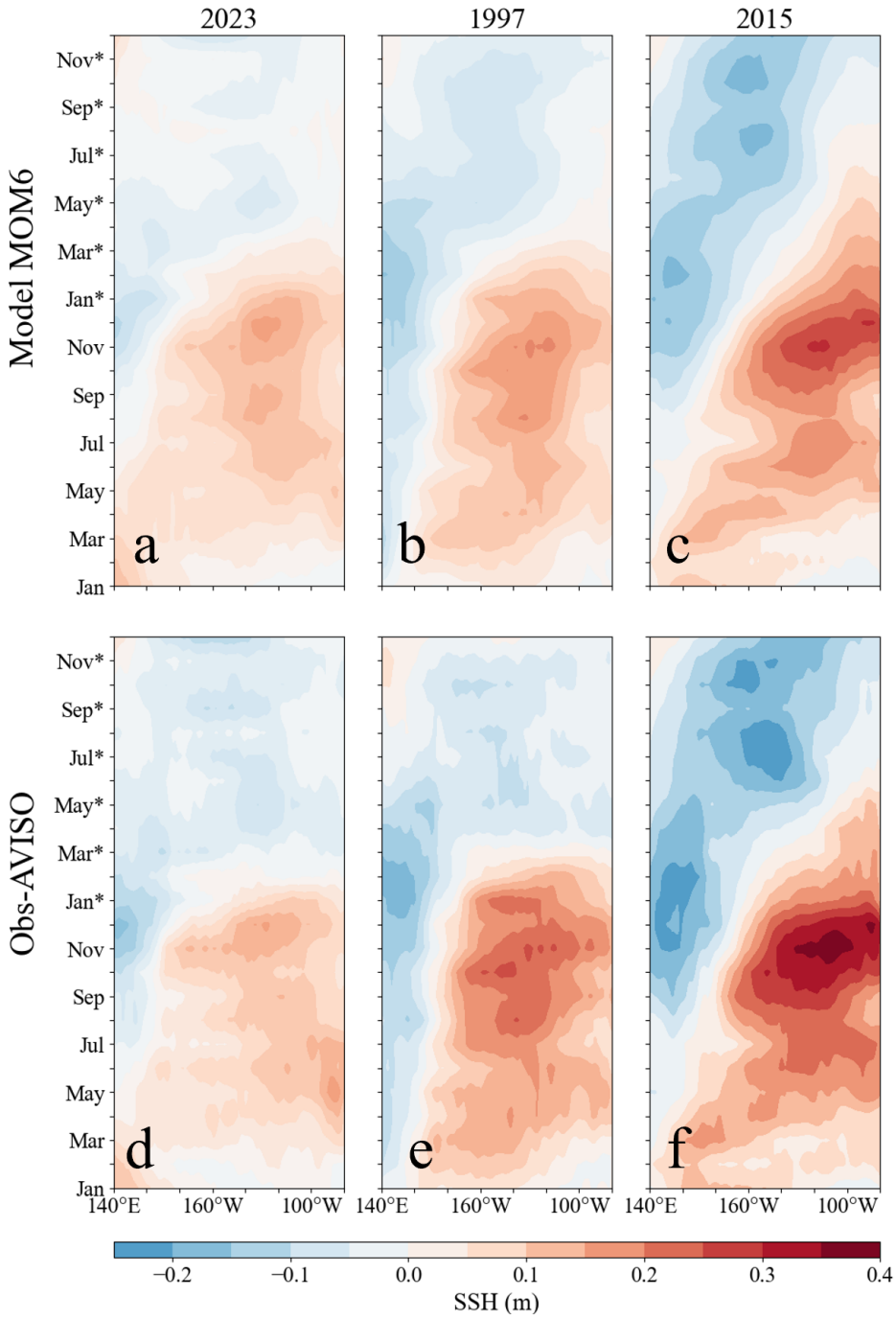



**Figure S16.** Hovmöller diagrams showing the longitude–time evolution of equatorial SSH anomalies (140°E–80°W, averaged over 2°S–2°N) during the (a) 2023, (b) 1997, and (c) 2015 El Niño events from MOM6-COBALT2 simulations, and the corresponding (d–f) AVISO observations (Ducet et al., 2000). The time axis spans January of the El Niño onset year to December of the following year (e.g., Jan 2023–Dec 2024 for the 2023 event). Months marked with "*" denote the second year of the event, while months without "*" correspond to the onset year.

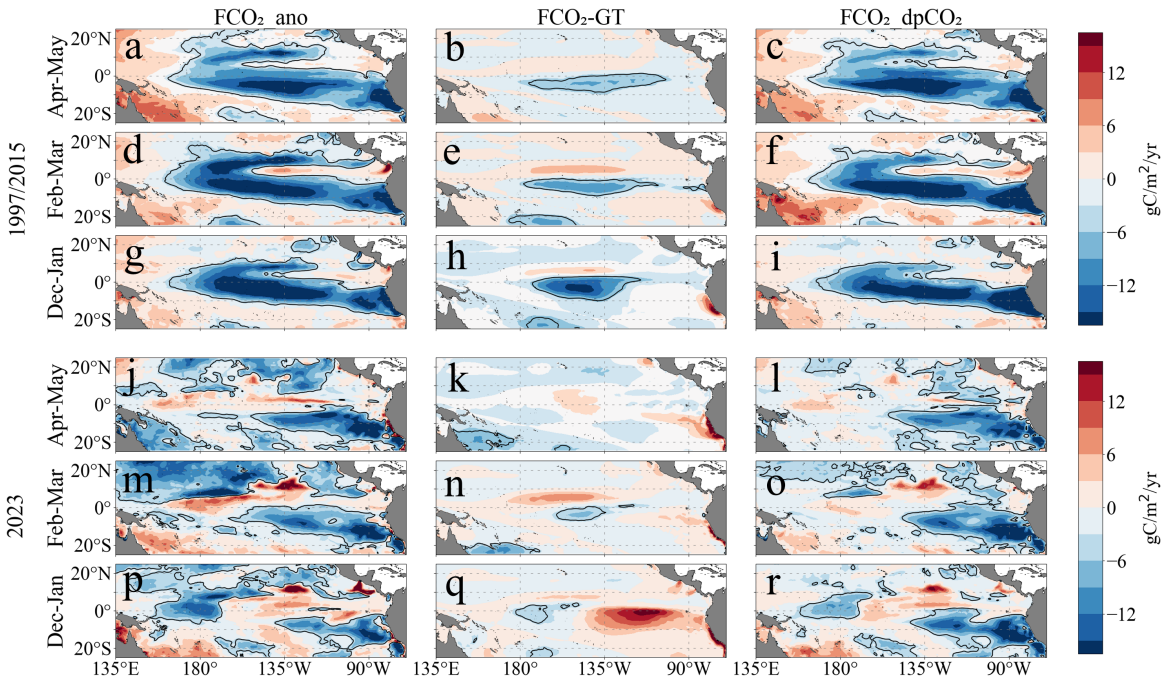



**Figure S17.** Spatial distribution of $FCO_2$ and its decompositions ($FCO_2$-GT, $FCO_2$-$\Delta pCO_2$) during the 2023 El Niño and other comparable events (1997/2015). Contours denote -5 gC/m$^2$/yr $FCO_2$ anomaly.

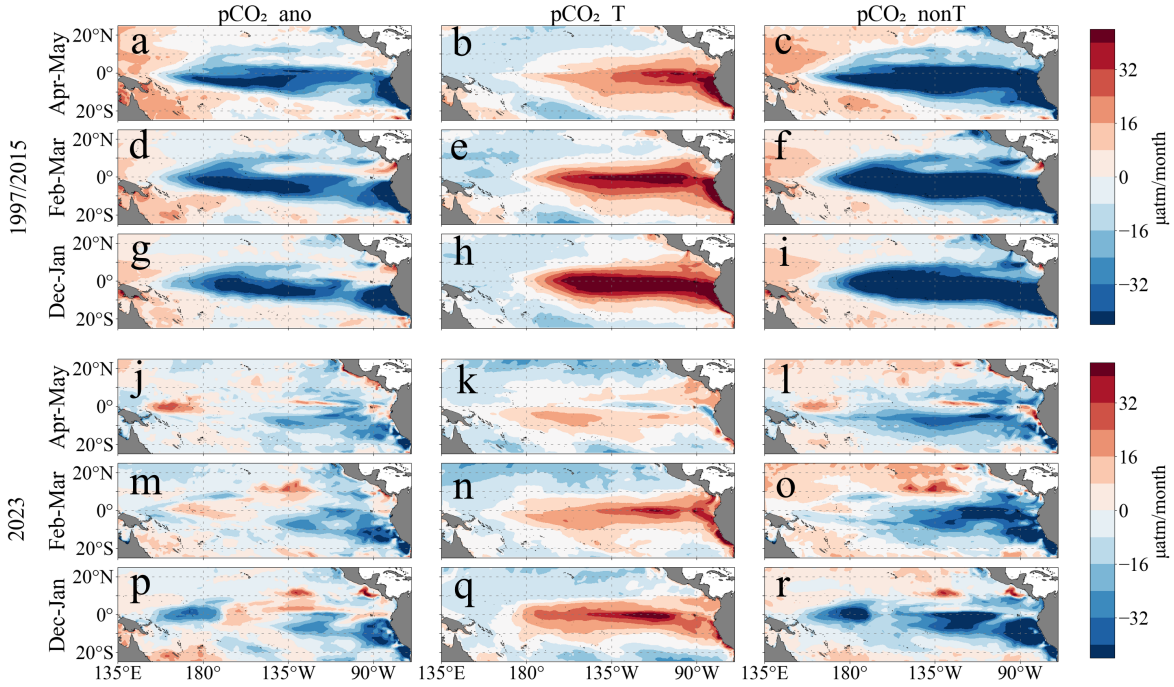



**Figure S18.** Spatial distribution of surface ocean $pCO_2$ and its thermal ($pCO_2$–T) and non-thermal ($pCO_2$–nonT) components during the 2023 El Niño, compared with the 1997 and 2015 El Niño events.

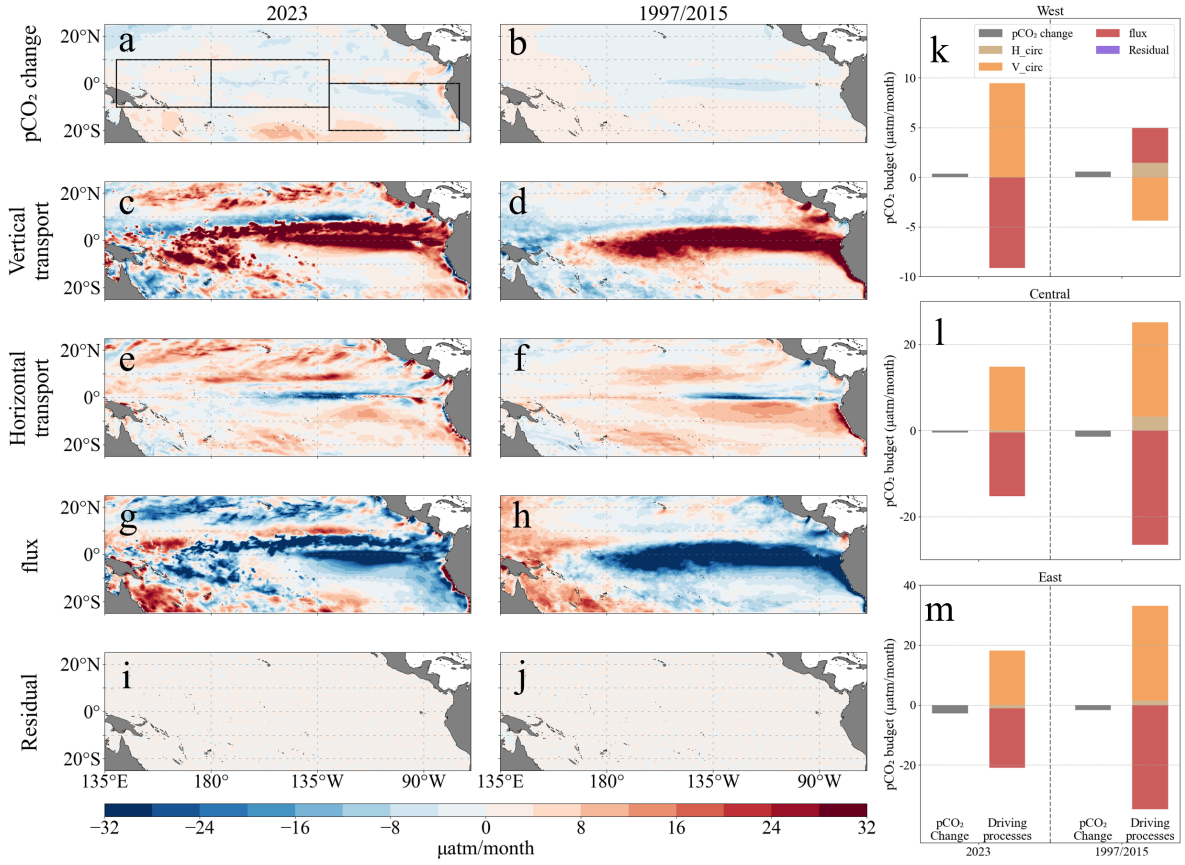



**Figure S19.** Thermal-driven ocean $pCO_2$ anomaly budget in the tropical Pacific during the 2023 El Niño and comparable extreme events (1997/2015), based on Eq. S13. (a, b) Spatial distribution of thermal $pCO_2$ change for 2023 and 1997/2015, respectively. (c–j) Contributions of individual processes to $pCO_2$ variability. (k–m) Regional $pCO_2$ budget comparisons between 2023 and 1997/2015 for the western, central, and eastern tropical Pacific, as indicated in (a). The western basin is defined as 140°E–180°E, 10°S–10°N, the central basin as 180°W–130°W, 10°S–10°N, and the eastern basin as 130°W–70°W, 20°S–0°N. All anomalies are computed as the December–February mean of monthly anomalies from MOM6-COBALT2.

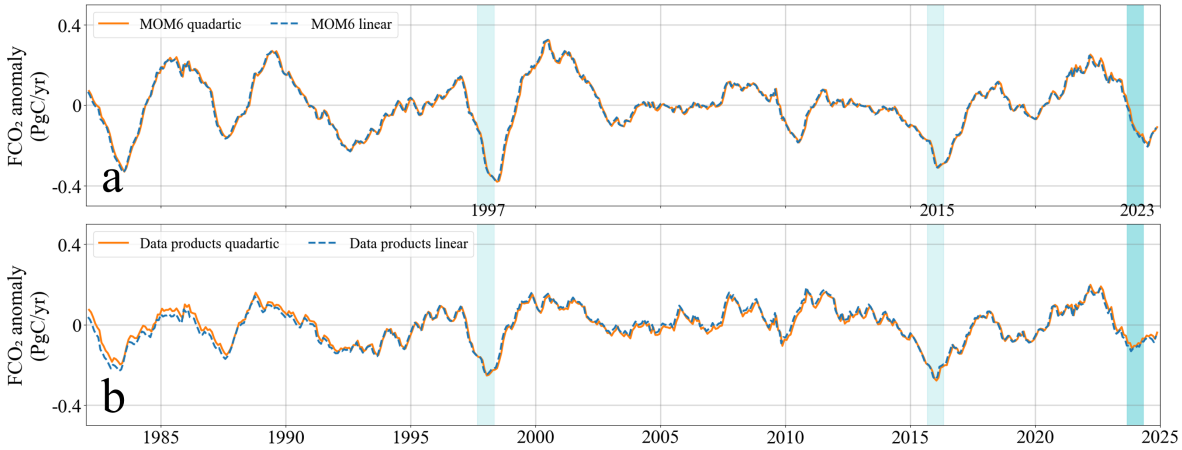



**Figure S20.** Time series of tropical Pacific $FCO_2$ anomalies derived from (a) MOM6 simulations and (b) observational data products. The anomalies are integrated over the tropical Pacific (160°E–285°E, 15°S–15°N) for the period 1982–2025. Orange lines denote linearly detrended anomalies, while blue dashed lines indicate quadratically detrended results.

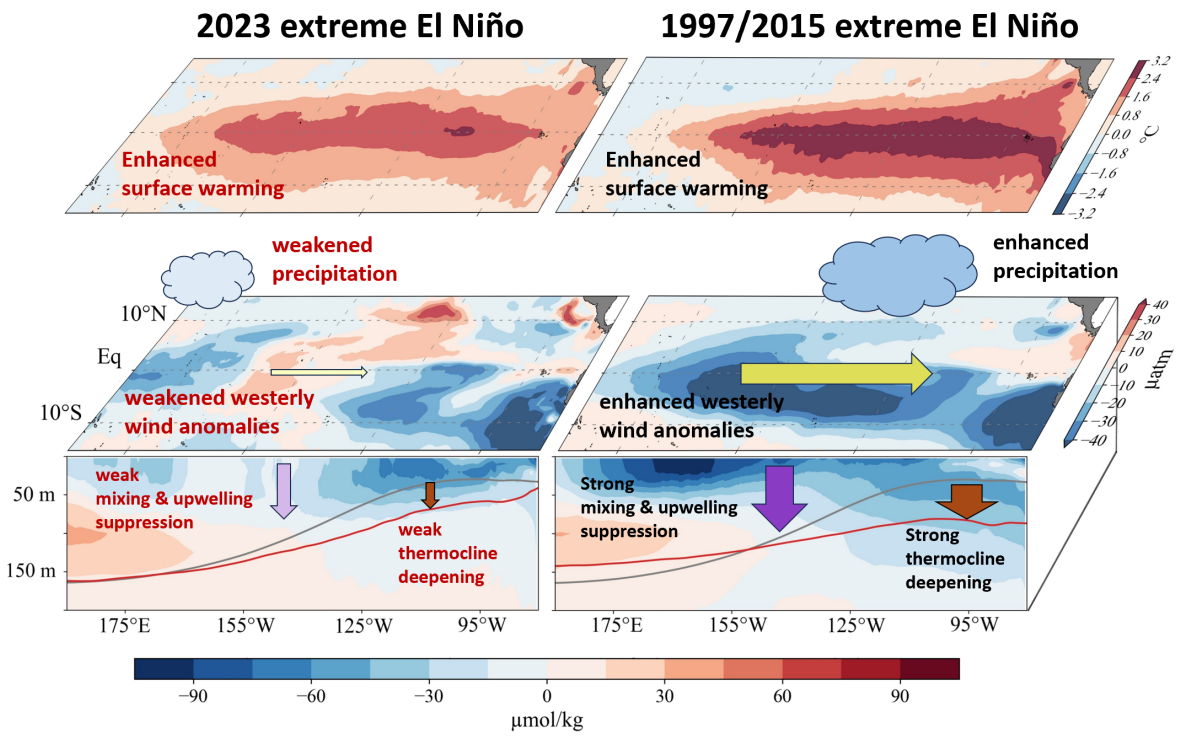



**Figure S21.** Schematic comparison of the mechanisms driving the tropical Pacific carbon cycle response during the 2023 El Niño and other comparable strong El Niño events. The map panels show SST (upper) and sea surface $pCO_2$ (lower) anomalies, while the vertical sections illustrate DIC concentration anomalies and thermocline depth relative to climatology. Arrows indicate the key processes involved, including changes in precipitation patterns, wind anomalies, freshwater flux, vertical mixing and upwelling, and thermocline adjustments.

# References


Adcroft, A., W. Anderson, V. Balaji, C. Blanton, M. Bushuk, C. O. Dufour, J. P. Dunne, S. M. Griffies, R. Hallberg, M. J. Harrison, I. M. Held, M. F. Jansen, J. G. John, J. P. Krasting, A. R. Langenhorst, S. Legg, Z. Liang, C. McHugh, A. Radhakrishnan, B. G. Reichl, T. Rosati, B. L. Samuels, A. Shao, R. Stouffer, M. Winton, A. T. Wittenberg, B. Xiang, N. Zadeh, and R. Zhang (2019). The gfdl global ocean and sea ice model om4.0: Model description and simulation features. *Journal of Advances in Modeling Earth Systems 11*(10), 3167–3211.

Aumont, O., C. Ethe, A. Tagliabue, L. Bopp, and M. Gehlen (2015). Pisces-v2: an ocean biogeochemical model for carbon and ecosystem studies. *Geoscientific Model Development 8*(8), 2465–2513.

Bakker, D. C. E., B. Pfeil, C. S. Landa, N. Metzl, K. M. O'Brien, A. Olsen, K. Smith, C. Cosca, S. Harasawa, S. D. Jones, S. Nakaoka, Y. Nojiri, U. Schuster, T. Steinhoff, C. Sweeney, T. Takahashi, B. Tilbrook, C. Wada, R. Wanninkhof, S. R. Alin, C. F. Balestrini, L. Barbero, N. R. Bates, A. A. Bianchi, F. Bonou, J. Boutin, Y. Bozec, E. F. Burger, W.-J. Cai, R. D. Castle, L. Chen, M. Chierici, K. Currie, W. Evans, C. Featherstone, R. A. Feely, A. Fransson, C. Goyet, N. Greenwood, L. Gregor, S. Hankin, N. J. Hardman-Mountford, J. Harlay, J. Hauck, M. Hoppema, M. P. Humphreys, C. W. Hunt, B. Huss, J. S. P. Ibánhez, T. Johannessen, R. Keeling, V. Kitidis, A. Körtzinger, A. Kozyr, E. Krasakopoulou, A. Kuwata, P. Landschützer, S. K. Lauvset, N. Lefèvre, C. Lo Monaco, A. Manke, J. T. Mathis, L. Merlivat, F. J. Millero, P. M. S. Monteiro, D. R. Munro, A. Murata, T. Newberger, A. M. Omar, T. Ono, K. Paterson, D. Pearce, D. Pierrot, L. L. Robbins, S. Saito, J. Salisbury, R. Schlitzer, B. Schneider, R. Schweitzer, R. Sieger, I. Skjelvan, K. F. Sullivan, S. C. Sutherland, A. J. Sutton, K. Tadokoro, M. Telszewski, M. Tuma, S. M. A. C. van Heuven, D. Vandemark, B. Ward, A. J. Watson, and S. Xu (2016). A multi-decade record of high-quality $fco_2$ data in version 3 of the surface ocean $co_2$ atlas (socat). *Earth System Science Data 8*(2), 383–413.

Bennington, V., L. Gloege, and G. A. McKinley (2022). Variability in the global ocean carbon sink from 1959 to 2020 by correcting models with observations. *Geophysical Research Letters 49*(12), e2022GL098632.

Berthet, S., R. Séférian, et al. (2019). Evaluation of an online ocean biogeochemical model in cnrm-esm2-1. *Journal of Advances in Modeling Earth Systems*.

Chau, T.-T.-T., M. Gehlen, N. Metzl, and F. Chevallier (2024). Cmems-lsce: a global, 0.25°, monthly reconstruction of the surface ocean carbonate system from 1985 onward. *Earth System Science Data 16*, 121–151.

Doney, S. C., V. J. Fabry, R. A. Feely, and J. A. Kleypas (2009). Ocean acidification: The other co2 problem. *Annual Review of Marine Science 1*, 169–192.

Ducet, N., P. Y. Le Traon, and G. Reverdin (2000). Global high-resolution mapping of ocean circulation from topex/poseidon and ers-1 and -2. *Journal of Geophysical Research: Oceans 105*(C8), 19477–19498.

Ford, D. J., J. Blannin, J. Watts, A. J. Watson, P. Landschützer, A. Jersild, and J. D. Shutler (2024). A comprehensive analysis of air-sea co2 flux uncertainties constructed from surface ocean data products. *Global Biogeochemical Cycles 38*(11), e2024GB008188.

Friedlingstein, P., M. O'Sullivan, M. W. Jones, R. M. Andrew, J. Hauck, P. Landschützer, C. Le Quéré, H. Li, I. T. Luijkx, A. Olsen, G. P. Peters, W. Peters, J. Pongratz, C. Schwingshackl, S. Sitch, J. G. Canadell, P. Ciais, R. B. Jackson, S. R. Alin, A. Arneth, V. Arora, N. R. Bates, M. Becker, N. Bellouin, C. F. Berghoff, H. C. Bittig, L. Bopp, P. Cadule, K. Campbell, M. A. Chamberlain, N. Chandra, F. Chevallier, L. P. Chini, T. Colligan, J. Decayeux, L. M. Djeutchouang, X. Dou, C. Duran Rojas, K. Enyo, W. Evans, A. R. Fay, R. A. Feely, D. J. Ford, A. Foster, T. Gasser, M. Gehlen, T. Gkritzalis, G. Grassi, L. Gregor, N. Gruber, O. Gürses, I. Harris, M. Hefner, J. Heinke, G. C. Hurtt, Y. Iida, T. Ilyina, A. R. Jacobson, A. K. Jain, T. Jarníková, A. Jersild, F. Jiang, Z. Jin, E. Kato, R. F. Keeling, K. Klein Goldewijk, J. Knauer, J. I. Korsbakken, X. Lan, S. K. Lauvset, N. Lefèvre, Z. Liu, J. Liu, L. Ma, S. Maksyutov, G. Marland, N. Mayot, P. C. McGuire, N. Metzl, N. M. Monacci, E. J. Morgan, S.-I. Nakaoka, C. Neill, Y. Niwa, T. Nützel, L. Olivier, T. Ono, P. I. Palmer, D. Pierrot, Z. Qin, L. Resplandy, A. Roobaert, T. M. Rosan, C. Rödenbeck, J. Schwinger, T. L. Smallman, S. M. Smith, R. Sospedra-Alfonso, T. Steinhoff, Q. Sun, A. J. Sutton, R. Séférian, S. Takao, H. Tatebe, H. Tian, B. Tilbrook, O. Torres, E. Tourigny, H. Tsujino, F. Tubiello, G. van der Werf, R. Wanninkhof, X. Wang, D. Yang, X. Yang, Z. Yu, W. Yuan, X. Yue, S. Zaehle, N. Zeng, and J. Zeng (2025). Global carbon budget 2024. *Earth System Science Data 17*(3), 965–1039.

Garcia, H. E., R. A. Locarnini, T. P. Boyer, J. I. Antonov, O. K. Baranova, M. M. Zweng, J. R. Reagan, and D. R. Johnson (2013a). *World Ocean Atlas 2013, Volume 3: Dissolved Oxygen, Apparent Oxygen Utilization, and Oxygen Saturation*. NOAA Atlas NESDIS 75. Silver Spring, MD: National Oceanographic Data Center (U.S.), Ocean Climate Laboratory.

Garcia, H. E., R. A. Locarnini, T. P. Boyer, J. I. Antonov, O. K. Baranova, M. M. Zweng, J. R. Reagan, and D. R. Johnson (2013b). *World Ocean Atlas 2013, Volume 4: Dissolved Inorganic Nutrients (phosphate, nitrate, silicate)*. NOAA Atlas NESDIS

76. Silver Spring, MD: National Oceanographic Data Center (U.S.), Ocean Climate Laboratory.

Gregor, L. and N. Gruber (2021). Oceansoda-ethzv2: a global gridded data set of the surface ocean carbonate system for seasonal to decadal studies of ocean acidification.

Gregor, L., A. D. Lebehot, S. Kok, and P. M. S. Monteiro (2019). A comparative assessment of the uncertainties of global surface ocean co2 flux estimates using a machine-learning ensemble (csir-ml6). *Geoscientific Model Development 12*, 5113–5135.

Gürses, , L. Oziel, O. Karakuş, D. Sidorenko, C. Voelker, Y. Ye, M. Zeising, M. Butzin, and J. Hauck (2023, 08). Ocean biogeochemistry in the coupled ocean–sea ice–biogeochemistry model fesom2.1–recom3. *Geoscientific Model Development 16*, 4883–4936.

Holte, J., L. D. Talley, J. Gilson, and D. Roemmich (2017). An argo mixed layer climatology and database. *Geophysical Research Letters 44*(11), 5618–5626.

Huang, B., C. Liu, V. Banzon, E. Freeman, G. Graham, B. Hankins, T. Smith, and H.-M. Zhang (2021a). Improvements of the daily optimum interpolation sea surface temperature (doisst) version 2.1. *Journal of Climate 34*(8), 2923 – 2939.

Huang, B., C. Liu, V. Banzon, E. Freeman, G. Graham, B. Hankins, T. Smith, and H.-M. Zhang (2021b). Improvements of the daily optimum interpolation sea surface temperature (doisst) version 2.1. *Journal of Climate 34*(8), 2923 – 2939.

Iida, Y., Y. Takatani, A. Kojima, and M. Ishii (2015). Global trends of ocean co2 sink and ocean acidification: an observation-based reconstruction of surface ocean inorganic carbon variables. *Journal of Oceanography 71*(4), 449–468.

Khatiwala, S., T. Tanhua, S. Mikaloff Fletcher, M. Gerber, S. C. Doney, H. D. Graven, N. Gruber, G. A. McKinley, A. Murata, A. F. Ríos, and C. L. Sabine (2013). Global ocean storage of anthropogenic carbon. *Biogeosciences 10*(4), 2169–2191.

Lacroix, F., T. Ilyina, M. Mathis, G. G. Laruelle, and P. Regnier (2021). Historical increases in land-derived nutrient inputs may alleviate effects of a changing physical climate on the oceanic carbon cycle. *Global Biogeochemical Cycles 35*(11).

Landschützer, P., G. G. Laruelle, A. Roobaert, and P. Regnier (2020). A uniform pco2 climatology combining open and coastal oceans. *Earth System Science Data 12*(4), 2537–2553.

Lauvset, S. K., N. Lange, T. Tanhua, H. C. Bittig, A. Olsen, A. Kozyr, S. Alin, M. Álvarez, K. Azetsu-Scott, L. Barbero, S. Becker, P. J. Brown, B. R. Carter, L. C. da Cunha, R. A. Feely, M. Hoppema, M. P. Humphreys, M. Ishii, E. Jeansson, L.-Q. Jiang, S. D. Jones, C. Lo Monaco, A. Murata, J. D. Müller, F. F. Pérez, B. Pfeil, C. Schirnick, R. Steinfeldt, T. Suzuki, B. Tilbrook, A. Ulfsbo, A. Velo, R. J. Woosley, and R. M. Key (2022). Glodapv2.2022: the latest version of the global interior ocean biogeochemical data product. *Earth System Science Data 14*(12), 5543–5572.

Law, R. M., T. Ziehn, R. J. Matear, A. Lenton, M. A. Chamberlain, L. E. Stevens, and Y.-P. Wang (2017). The carbon cycle in the australian community climate and earth system simulator (access-esm1). *Journal of Southern Hemisphere Earth Systems Science 67*(2), 101–129.

Le Quéré, C., J. C. Orr, P. Monfray, O. Aumont, and G. Madec (2000). Interannual variability of the oceanic sink of co2 from 1979 through 1997. *Global Biogeochemical Cycles 14*(4), 1247–1265.

Liao, E., W. Lu, L. Xue, and Y. Du (2024). Weakening indian ocean carbon uptake in 2015: The role of amplified basin-wide warming and reduced indonesian throughflow. *Limnology and Oceanography Letters 9*(4), 442–451.

Liao, E., L. Resplandy, J. Liu, and K. W. Bowman (2020). Amplification of the ocean carbon sink during el niños: Role of poleward ekman transport and influence on atmospheric co2. *Global Biogeochemical Cycles 34*(9), e2020GB006574. e2020GB006574 2020GB006574.

Locarnini, R. A., A. V. Mishonov, J. I. Antonov, T. P. Boyer, H. E. Garcia, O. K. Baranova, M. M. Zweng, C. R. Paver, J. R. Reagan, D. R. Johnson, M. Hamilton, D. Seidov, and S. Levitus (2013). *World ocean atlas 2013. Volume 1, Temperature*. NOAA atlas NESDIS ; 73. Silver Spring, MD: National Oceanographic Data Center (U.S.), Ocean Climate Laboratory.

Lovenduski, N. S., N. Gruber, S. C. Doney, and I. D. Lima (2007). Enhanced co2 outgassing in the southern ocean from a positive phase of the southern annular mode. *Global Biogeochemical Cycles 21*(2).

McPhaden, M. J., A. J. Busalacchi, R. Cheney, J.-R. Donguy, K. S. Gage, D. Halpern, M. Ji, P. Julian, G. Meyers, G. T. Mitchum, P. P. Niiler, J. Picaut, R. W. Reynolds, N. Smith, and K. Takeuchi (1998). The tropical ocean-global atmosphere observing system: A decade of progress. *Journal of Geophysical Research: Oceans 103*(C7), 14169–14240.

Melnichenko, O., P. Hacker, N. Maximenko, G. Lagerloef, and J. Potemra (2016). Optimum interpolation analysis of aquarius sea surface salinity. *Journal of Geophysical Research: Oceans 121*(1), 602–616.

Najjar, R. and J. Orr (1998). Design of ocmip-2 simulations of chlorofluorocarbons, the solubility pump and common biogeochemistry. Technical Report 19, Internal OCMIP Report, LSCE/CEA Saclay, Gif-sur-Yvette, France.

Rödenbeck, C., T. DeVries, J. Hauck, C. Le Quéré, and R. F. Keeling (2022). Data-based estimates of interannual sea–air co2 flux variations 1957–2020 and their relation to environmental drivers. *Biogeosciences 19*, 2627–2652.

Sarmiento, J. L. and N. Gruber (2013). *Ocean Biogeochemical Dynamics*. Princeton: Princeton University Press.

Sathyendranath, S., R. J. Brewin, C. Brockmann, V. Brotas, B. Calton, A. Chuprin, P. Cipollini, A. B. Couto, J. Dingle, R. Doerffer, C. Donlon, M. Dowell, A. Farman, M. Grant, S. Groom, A. Horseman, T. Jackson, H. Krasemann, S. Lavender, V. Martinez-Vicente, C. Mazeran, F. Mélin, T. S. Moore, D. Müller, P. Regner, S. Roy, C. J. Steele, F. Steinmetz, J. Swinton, M. Taberner, A. Thompson, A. Valente, M. Zühlke, V. E. Brando, H. Feng, G. Feldman, B. A. Franz, R. Frouin, R. W. Gould, S. B. Hooker, M. Kahru, S. Kratzer, B. G. Mitchell, F. E. Muller-Karger, H. M. Sosik, K. J. Voss, J. Werdell, and T. Platt (2019). An ocean-colour time series for use in climate studies: The experience of the ocean-colour climate change initiative (oc-cci). *Sensors 19*(19).

Schwinger, J., N. Goris, J. F. Tjiputra, P. Köhler, A. Olsen, and M. Bentsen (2016). Evaluation of noresm-oc (versions 1 and 1.2), the ocean carbon-cycle stand-alone configuration of the norwegian earth system model (noresm1). *Geoscientific Model Development 9*, 2589–2622.

Séférian, R., P. Nabat, M. Michou, D. Saint-Martin, A. Voldoire, J. Colin, B. Decharme, C. Delire, et al. (2019). Evaluation of cnrm earth system model, cnrm-esm2-1: role of earth system processes in present-day and future climate. *Journal of Advances in Modeling Earth Systems 11*(12), 4182–4227.

Stock, C. A., J. P. Dunne, S. Fan, P. Ginoux, J. John, J. P. Krasting, C. Laufkötter, F. Paulot, and N. Zadeh (2020). Ocean biogeochemistry in gfdl's earth system model 4.1 and its response to increasing atmospheric co2. *Journal of Advances in Modeling Earth Systems 12*(10), e2019MS002043.

Stock, C. A., J. P. Dunne, and J. G. John (2014). Global-scale carbon and energy flows through the marine planktonic food web: An analysis with a coupled physical–biological model. *Progress in Oceanography 120*, 1–28.

Sun, C., E. Liao, and X. Zhu (2025). Asymmetrical ocean carbon responses in the tropical pacific ocean to la niña and el niño. *Geophysical Research Letters 52*(4), e2024GL112039. e2024GL112039 2024GL112039.

Sutton, A. J., C. L. Sabine, S. Maenner-Jones, N. Lawrence-Slavas, C. Meinig, R. A. Feely, J. T. Mathis, S. Musielewicz, R. Bott, P. D. McLain, H. J. Fought, and A. Kozyr (2014). A high-frequency atmospheric and seawater $pco_2$ data set from 14 open-ocean sites using a moored autonomous system. *Earth System Science Data 6*(2), 353–366.

Takahashi, T., J. Olafsson, J. G. Goddard, D. W. Chipman, and S. C. Sutherland (1993). Seasonal variation of co2 and nutrients in the high-latitude surface oceans: A comparative study. *Global Biogeochemical Cycles 7*(4), 843–878.

Tsuji, N., J. L. Kennemur, T. Buyck, S. Lee, S. Prévost, P. S. J. Kaib, D. Bykov, C. Farès, and B. List (2018). Activation of olefins via asymmetric brønsted acid catalysis. *Science 359*(6383), 1501–1505.

Tsujino, H., S. Urakawa, S. M. Griffies, et al. (2020). Mri-esm2.0: The meteorological research institute earth system model version 2.0. *Journal of Advances in Modeling Earth Systems 12*(1).

Wanninkhof, R., G.-H. Park, T. Takahashi, C. Sweeney, R. Feely, Y. Nojiri, N. Gruber, S. C. Doney, G. A. McKinley, A. Lenton, C. Le Quéré, C. Heinze, J. Schwinger, H. Graven, and S. Khatiwala (2013). Global ocean carbon uptake: magnitude, variability and trends. *Biogeosciences 10*(3), 1983–2000.

Weiss, R. and B. Price (1980). Nitrous oxide solubility in water and seawater. *Marine Chemistry 8*(4), 347–359.

Wright, R. M., E. T. Buitenhuis, S. Pitois, and C. Le Quéré (2021). Role of jellyfish in the plankton ecosystem revealed using a global ocean biogeochemical model. *Biogeosciences 18*, 1291–1320.

Zeng, J. (2022). Nies-ml3 ensemble product of surface ocean co2 concentrations and air-sea co2 fluxes reconstructed by using three machine learning models with new co2 trends.

Zhang, X., E. Liao, W. Lu, Z. Wu, G. Wang, X. Zhu, and S. Liang (2025). A surface ocean $pco_2$ product with improved representation of interannual variability using a vision transformer-based model. *Earth System Science Data Discussions 2025*, 1–35.

Zweng, M. M., J. R. Reagan, J. I. Antonov, R. A. Locarnini, A. V. Mishonov, T. P. Boyer, H. E. Garcia, O. K. Baranova, D. R. Johnson, and D. Seidov (2013). *World Ocean Atlas 2013, Volume 2: Salinity*. NOAA Atlas NESDIS 74. Silver Spring, MD: National Oceanographic Data Center (U.S.), Ocean Climate Laboratory.